Ultrasonic guided wave monitoring of dendrite formation at electrode–electrolyte interface in aqueous zinc ion batteries

Yifeng Zhang [a,1], Haobo Dong [b,1], Tianlei Wang [b], Guanjie He [b,*], Ivan P. Parkin [b,*], Frederic Cegla [a,*]
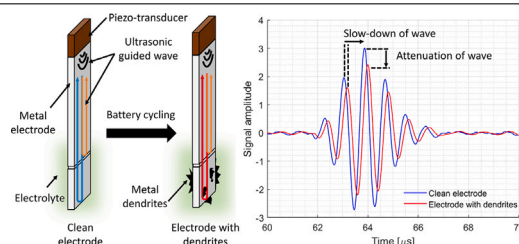
[a] NDE Group, Department of Mechanical Engineering, Imperial College London, Exhibition Road, London SW7 2AZ, United Kingdom
[b] Christopher Ingold Laboratory, Department of Chemistry, University College London, 20 Gordon Street, London WC1H 0AJ, United Kingdom

HIGHLIGHTS

- Dendrite formation on electrode surfaces is a key degradation process in batteries.
- A novel technique for in-situ monitoring of dendrite formation is presented.
- Properties of guided ultrasonic waves are affected by the dendrites.
- Technique delivers quantitative insights into battery degradation processes.

GRAPHICAL ABSTRACT

ARTICLE INFO

ABSTRACT

The formation of dendrite affects the cycling life of a battery and lead to malfunctions such as internal short-circuiting and thermal runaway events. However, existing methods to observe dendrite formation, such as X-ray computed tomography and scanning electron microscopy are either prohibitively complicated or unsuitable for long-term, *in-situ* monitoring. In this study we present a method which uses the fundamental shear-horizontal mode (SH0*) guided ultrasonic waves to independently monitor the status of the electrodes in a symmetric aqueous zinc-ion battery. Experimental measurements show that the velocity and attenuation of the ultrasonic wave on the opposing electrodes vary in the opposite senses during the cycling. While the velocity and attenuation changes can be partially reversed, a monotonic drift can also be observed with increasing number of cycles. Coupled with optical microscopy, the partially reversible oscillations can be associated with zinc stripping/plating. The irreversible drifting can be associated with the formation of 'dead' zinc dendrite. The technique shows clear sensitivity to the formation of dendrite, especially in the early stages (∼10 cycles) of charging and discharging processes. This work should inspire future research to enable quantitative assessment of the technique sensitivity and to improve its resolution.

1. Introduction

With a clear target for economies to become carbon neutral in the foreseeable future, energy storage devices have attracted a lot of attention over the last decade. Among them, aqueous zinc-ion batteries are regarded as potential candidate for large scale grid/off-grid energy storage batteries owing to the high theoretical energy storage capacity of zinc ($5855 \, \mathrm{mAhcm^{-3}}$) [1] and its ease of manufac-turing. Compared to lithium-ion batteries, the relative low price of $ 25 \, \mathrm{kg^{-1}}$ [2] and inflammability also increases its attractiveness. For most rechargeable zinc-based batteries, no matter whether alkaline or acidic, metal plating/striping occurs on the zinc anode during galvanic charging/discharging processes. In a full cell, zinc ions in the aqueous electrolyte will receive two electrons so that zinc is deposited onto the
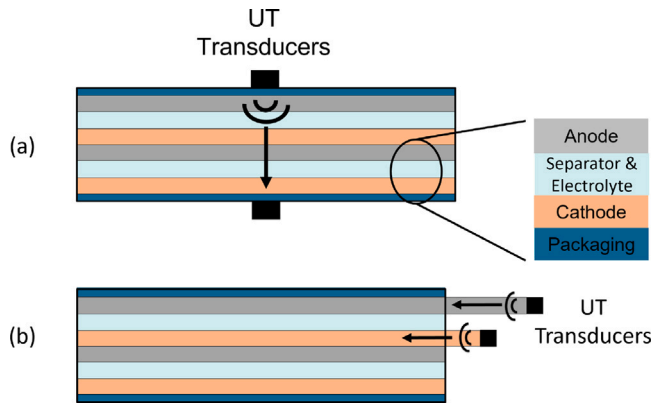

Fig. 1. Comparison of (a) traditional ultrasonic testing setup where waves travel across a stack of cathodes, separators and anodes; (b) the setup used in this study where ultrasonic guided waves travel along the electrodes that form an ultrasonic waveguide.

anode during the charging process, while zinc ions will be stripped from the anode and passed into the electrolyte during discharging. Theoretically, it is a highly reversible reaction where the zinc metal is the source of zinc ions in the electrolyte which also acts as the conductive medium. However, because of pH variations or uneven electric fields, zinc dendrites often form on the zinc anode as a by-product [3,4]. The formation of dendrites not only affects the coulombic efficiency and capacity retention of a battery [5], but may also lead to safety issues such as internal short-circuiting and thermal runaway of the battery [6].

Currently, zinc dendrites are usually monitored by X-ray computed tomography (CT), scanning electron microscope (SEM) or atomic force microscopy (AFM) [7–9]. However, these existing methods are either prohibitively complicated or unsuitable for long-term, real-time, *in-situ/-operando* monitoring. Recently, ultrasonic testing (UT) has become an alternative method for monitoring the health and status of battery cells. Several researchers have investigated the correlations between acoustic signals and the electrochemical and mechanical properties of commercial lithium-ion pouch cells [10–14]. In most of the previous research, ultrasonic waves were excited to propagate across the thickness of the battery, thereby penetrating through multiple layers of anodes, cathodes and electrolytes (Fig. 1(a)). Although such a setup is relatively easy to employ, it also has some obvious drawbacks: (1) ultrasonic reflections from the interfaces between cathode, anode, separator and electrolyte superimpose and are heavily attenuated, hence the received signals are difficult to interpret. (2) the cathode and anode material are under different ion insertion mechanism which is difficult to discern in the received ultrasonic signals due to the superposition of the reflected waves [15]. Hence, most of the previous work seeks to correlate the State-of-Charge (SoC) or State-of-Health (SoH) of batteries with changes in the ultrasonic signals and arrives at qualitative conclusions.

In this study, we present a novel method which uses a guided wave to interrogate individual cathodes and anodes separately (Fig. 1(b)), thereby allowing much higher sensitivity to the physical changes that take place on the electrode surfaces.

2. Methodology

2.1. Ultrasonic sensing principles

Two characteristics of elastic waves, velocity and attenuation, are used in this study as features to monitor the extent of dendrite formation on electrode surfaces. The velocity of shear ultrasonic waves in a clean (unloaded) waveguide is related to its shear modulus G and density ρ_s by the following equation:

$$c_0 = \sqrt{\frac{G}{\rho_s}} \qquad (1)$$

Fig. 2(a) shows the design of the transducer-waveguide assembly used in this study. The waveguide was made of zinc and was 80 mm long, 15 mm wide and 0.5 mm thick. The surface of the waveguide was lightly grinded with P2500 silicon carbide abrasive papers and cleaned with acetone. A piezo-electric transducer (PZT) was bonded to one end cross-section (15 mm × 0.5 mm). A notch was engraved on one of the broad surfaces (80 mm × 15 mm) at 20 mm from the end that was furthest away from the transducer. This is used to define the "measurement section" for which the ultrasonic characteristics are measured. The transducer produces elastic waves that mainly consist of the non-dispersive, fundamental shear-horizontal (SH0*) mode [16]. As the SH0* wave propagates along the waveguide, it is partially reflected at the notch and this is the first echo that returns to the transducer as shown in Fig. 2(b); the remaining energy of the outgoing SH0* wave is then completely reflected at the end of the waveguide and most of it is received by the transducer as the second echo. The separation in time between the first and second echo is the time-of-flight (ToF) of the SH0* wave travelling through twice the length of the 'measurement section'. The velocity of the SH0* mode over the measurement section, c_{ms}, can be calculated by

$$c_{ms} = \frac{2x}{t_{ToF}} \qquad (2)$$

Different from many of the previous research, wave attenuation was selected here over the more commonly used signal amplitude/intensity as the second feature for monitoring battery/electrode conditions. Ultrasonic signal amplitude/intensity is normally presented in arbitrary units (a.u.) as its value is affected by many parameters, including sensor output, temperature fluctuation, and measurement amplification etc.[17] Since this technique is intended for long-term and *in-operando* monitoring, factors such as sensor deterioration will be a key concern for its application. In contrast, wave attenuation bears physical meaning and is closely related to the conditions of the wave-bearing material, e.g. the conditions at the electrode–electrolyte interfaces. Wave attenuation in this study is determined by comparing the amplitude ratio of the first and second echoes, A_1 and A_2. This removes the effects on signal variation due to sensor output or amplification fluctuations.

As shown in Fig. 2(a), when a dendrite-free waveguide is immersed to a depth of d in the electrolyte, assuming the electrolyte is close to an inviscid liquid, wave attenuation, α, is only a result of the reflection coefficient of the wave on the notch and the material attenuation in the waveguide.

$$\alpha = -\frac{\ln(\frac{A_1}{A_2})}{2x} \qquad (3)$$

When dendrites are present on the electrode surface, the acoustic attenuation can be expressed by the following equation, [18]

$$\alpha' = -\frac{\ln(\frac{A_1 e^{-\alpha_d * 2(d-x)}}{A_2 e^{-\alpha_d * 2d}})}{2x} \qquad (4)$$

where α_d is the additional wave attenuation due to the presence of dendrites. Rearranging Eq.(3) and (4), the value of α_d can be calculated by

$$\alpha_d = \alpha - \alpha' \qquad (5)$$

Fig. 2(c) shows a typical ultrasonic signal acquired from a waveguide before and after dendrite has grown on the surface. Two noticeable differences can be identified from the graph: (1) a reduced signal amplitude suggests increased wave attenuation, due to additional energy loss that is caused by the presence of the dendrite. (2) a delayed arrival time of the ultrasound wave suggests reduced wave velocity.
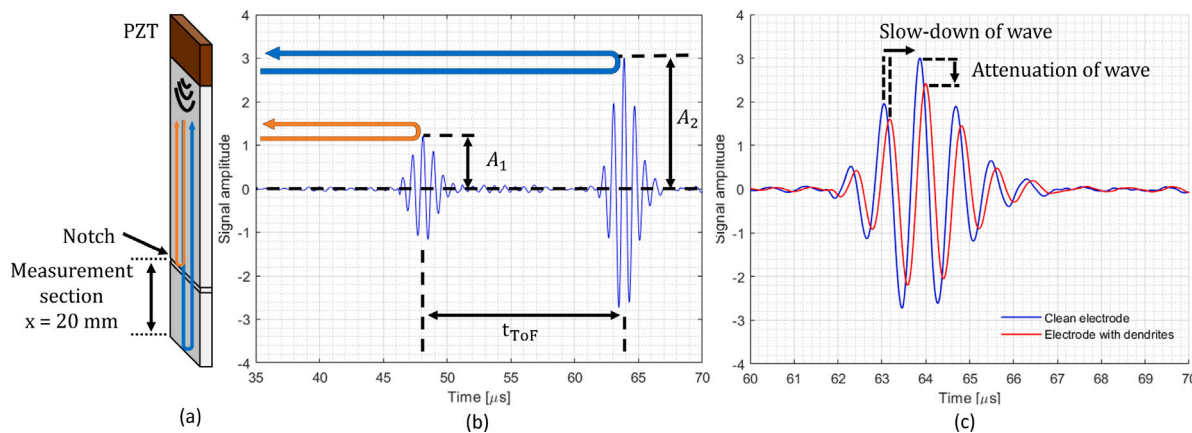
Fig. 2. (a) Schematic of a transducer-waveguide assembly. (b) Sample ultrasonic signals showing the reflected echoes from the notch and the waveguide end. (c) Sample ultrasonic signals on a waveguide before (blue) and after (red) the cycling. (For interpretation of the references to colour in this figure legend, the reader is referred to the web version of this article.)

2.2. Experimental setup

Chronopotentiometric tests were performed on a purpose-built symmetric cell to ensure only zinc plating/stripping phenomena will occur on the electrodes (Fig. 3). Three zinc electrode–transducer assemblies were positioned 10 mm apart in a transparent cubic beaker containing 1 M of $ZnSO_4$ aqueous solution. The electrodes were immersed into the electrolyte by 25 mm and the immersed area of each electrode was approximately 3.75 cm². The three electrodes were named as the working electrode (WE), counter electrode (CE) and reference electrode (RE). The neighbouring working and counter electrode were connected to an external potentiostat (PalmSens 3, PalmSens BV, Randhoeve 221, 3995 GA Houten, the Netherlands) and together they formed a symmetric aqueous Zn ion battery. In contrast to conventional three-electrode tests, the reference electrode in this system did not take part in any electro-chemical reactions, however, it was used to log any changes in the ultrasonic signals caused by the environment such as temperature variations or corrosion.

Ultrasonic signals of 1.2 MHz were excited by piezo-electric PZT transducers on each of the three electrodes. The reflected signals were later received by the same PZT transducers and digitised at 50 MHz. The temperature of the electrolyte and the ambient air were measured by two resistance temperature detector (RTD) probes (RS PRO 2 wire PT1000 Sensor, class B, RS Components Ltd, Birchington Road, Corby, Northants, UK) and the measurements were sampled by a data logger (PT-104 Platinum Resistance Data Logger, Pico Technology, St Neots, Cambridgeshire, UK). An optical microscope (Jiusion, www.jiusion.com) with approximately 1000 times magnification was set up next to the beaker to observe the cross section of the counter electrode The area of view on the electrode cross section as shown in Fig. 3(c) was approximately 1000 μm × 500 μm, or roughly one twentieth of the entire cross-sectional area of the measurement section. The temperature, optical and ultrasonic measurements were sampled at a constant interval of 30 s. Voltage measurements across the electrodes were sampled at 100 Hz by the potentiostat.

Figure S1 (Appendix A: Supplementary Information) illustrates the electrochemical process that happens at the working and counter electrode. During the charging process, current flows from the counter electrode to the working electrode, thereby causing Zn in the working electrode to be stripped and passed into the electrolyte as Zn^{2+} ions. At the same time, Zn^{2+} ions in the electrolyte are reduced to Zn and deposit on the surface of the counter electrode. When the system enters the discharging state, current flows in the opposite direction and the electrochemical reactions that happen on the electrodes are also reversed.

$$Zn \longrightarrow Zn^{2+} + 2e^- \tag{6}$$

$$Zn^{2+} + 2e^- \longrightarrow Zn \tag{7}$$

2.3. Hypothesis and overview of experimental verification

We hypothesise that the SH0* guided wave is sensitive to dendrite formation at the electrode–electrolyte interface via two mechanisms: (1) zinc plating and dendrite build-up increased the effective mass and inertia of the electrode, which impedes the propagation of ultrasonic waves and reduces wave velocity. (2) the formation of zinc dendrites changes the morphology of the electrode surface and increases the mechanical coupling between the electrode and electrolyte. This increases the energy dissipation through the electrode–electrolyte interface and hence wave attenuation.

To verify this hypothesis, the following three-phase experiment was devised: In Phase I of the experiment (-1-h $< t <$ 0-h), the electrodes were immersed in the electrolyte without applying any electrical current. This is to establish a pre-cycling reference measurement. A constant current of 10 mA was applied to 'charge' and 'discharge' the cell in Phase II of the experiment (0-h $< t <$ 48-h). Each of the charging and discharging process was set to 1 h and the areal capacity of the cell is 2.67 mAhcm⁻². The cell was then rest for 1 h in Phase III of the experiment (48-h $< t <$ 49-h) to establish a post-cycling reference measurement.

3. Results and discussion

3.1. Evolution of ultrasonic wave attenuation and velocity

Following the protocol described earlier, Fig. 4(a) and (b) present the evolution of the ultrasonic wave attenuation and velocity on the three electrode. Fig. 4(c) and (d) show the across-electrode voltage differences and temperature variations during the experiment. Measurements taken on the working, counter and reference electrodes are shown in red, black and blue, respectively. The corresponding voltage–time profile during the experiment are shown in dark yellow. In this case the charge and discharge states correspond to the periods with positive and negative voltages, respectively. The voltage difference attained was in the range of ±0.1 V, which is a typical range for Zn//Zn half cell test under the given areal capacity.

Pre-cycling and post-cycling were performed to ensure that variations in the ultrasonic properties are the results of the electrochemical processes. In both Phase I (-1-h $< t <$ 0-h) and Phase III (48-h $< t <$ 49-h) of the experiment, attenuation and velocity evolution are relatively negligible on all three electrodes. In Phase II (0-h $< t <$ 48-h), variations in wave attenuation and velocity can be observed for both the working and counter electrode, while there is little change for the reference electrode. This contrast indicates that the variations in shear wave behaviours are mainly influenced by the battery cycling.
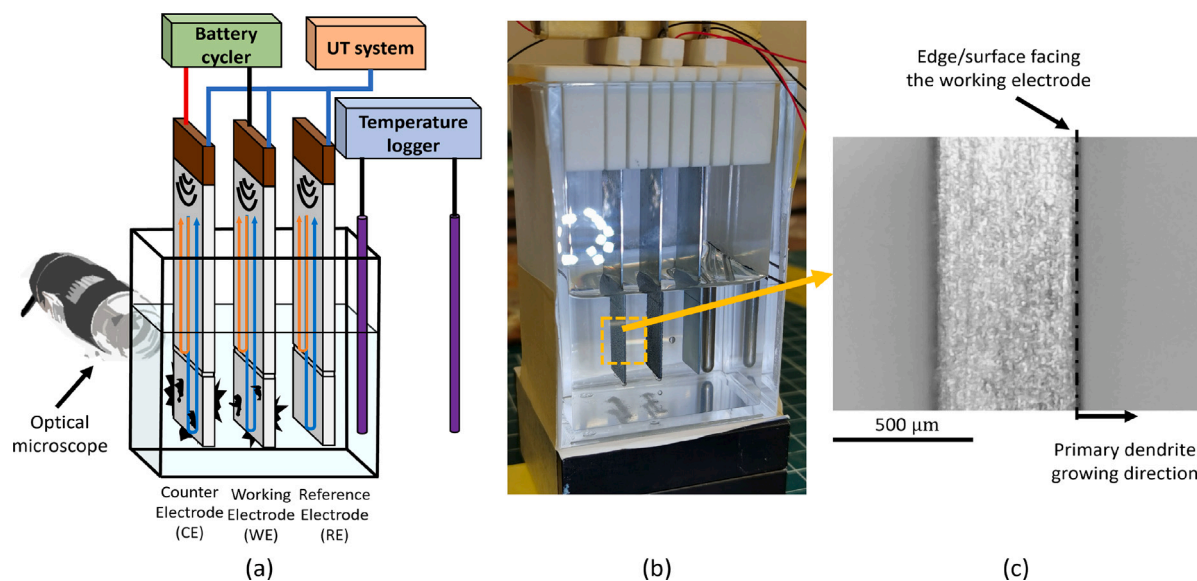
Fig. 3. (a) Schematic diagram of the experimental setup. (b) The actual experimental setup showing the three electrodes and the reaction vessel. (c) A sample optical image of the counter electrode.

In general, wave attenuation and velocity profile on the working and counter electrodes show cyclic behaviours. Wave attenuation on the opposing working and counter electrodes are observed to vary in the opposite sense and the variations depend on the state of the cell (i.e., current flowing direction/cross-electrode voltage difference). For example, when the cell was in the charging state, wave attenuation on the working electrode (from which Zinc is being stripped) reduced while the attenuation on the counter electrode (from which Zinc is being stripped) increased. The opposite occurs during discharge and the changes in attenuation were partially reversed. An irreversible monotonic drift can also be observed in the graph.

The evolution of wave velocity on the counter electrode is found to mirror that of wave attenuation. On the working electrode, the evolution of wave velocity is slightly more complicated: although opposite reactions occur on the working and counter electrode, wave velocity change on the working electrode is observed to be in phase/synchronised with that on the counter electrode in the early stage of Phase-II (c.a. 0-h $< t <$ 7-h). The profile of velocity variation on the working electrode then gradually evolved as the cycling proceeded. By c.a. t = 20-h the profile of wave velocity variations on the working electrode is observed to mirror that of velocity variations on the counter electrode.

Although the cycling experiment was carried out on a symmetric cell system, the ultrasonic measurements have shown some asymmetric behaviours between the working and counter electrode. For example, the accumulated wave attenuation and velocity variations on the working electrode are observed to be significantly larger than that on counter electrode, which suggest that more dendrites may have formed on the working electrode than on the counter electrode.

Some gas bubbles were observed on the working and counter electrodes during the experiment, however the gas bubbles were believed to have limited effects on the ultrasonic wave properties in this work. Gases trapped in a pouch-cell can severely interfere with conventional ultrasonic testing techniques because the impedance mismatch between the gas and electrode/electrolyte greatly attenuates ultrasonic waves travelling through them. In our study, the energy propagates along the electrode in the form of a guided wave, hence the wave does not rely on propagation through the gas that is formed on the electrode surface and therefore the wave is not substantially affected.

3.2. Correlation between ultrasonic measurements and zinc dendrite growth

Optical images of the counter electrode were taken during the experiment which confirms that the cyclic behaviour of SH0* wave corresponds to the growth and dissolution of zinc dendrites. Fig. 5 displays the optical images of the counter electrode in three specific charging–discharging cycles (cycle-1, -13, and -19). During each cycle, zinc dendrites began to grow on the electrode surface when the cell was being charged. 'Clusters' of zinc dendrites initiated/grew at various sites on the cross section and also along the right vertical edge of the electrode. The zinc dendrites then began to dissolve and diminish in size when the cell was subsequently being discharged. Comparing the initial and final states of the electrode, an increasing amount of undissolved zinc dendrite could be observed on the electrode surface with increasing number of cycles.

The height of zinc dendrites in the observed section was evaluated by tracking the tip of Zn dendrite along the right vertical edge of the electrode. An in-house tracking algorithm which uses a canny filter was implemented in MATLAB. As shown in Fig. 5, the red dash–dot line marks the boundary between the zinc substrate/dendrites complex and the electrolyte. The blue dashed line mark the initial position of the electrode edge at the start of the cycling at t = 0-h. The height of zinc dendrite (i.e. the thickness of the plated zinc layer) along the edge can be estimated by subtracting the initial position of the substrate edge from the locations of dendrite–electrolyte boundary. The calculated dendrite height distribution along the vertical edge is averaged over the number of pixels (550 pixels) and the evolution of average dendrite height on the counter electrode is presented in Fig. 4(e).

The evolution of dendrite height also shows cyclic behaviours with a monotonic increase over multiple cycles. The partially reversible dendrite growth and dissolution can be clearly observed within each charge–discharge cycle. The irreversible monotonic drift can be correlated with the accumulation of insoluble 'dead' zinc on the electrode surface as shown in Fig. 5. This corroborates that the algorithm is working as intended with the observed zinc plating and stripping phenomena. More importantly, the evolution of zinc dendrite height shows strong positive correlation with wave attenuation and strong inverse correlation wave velocity. The average dendrite height over the observed region is estimated to be 181 μm at t = 43-h. The image acquisition routine was disrupted and no image was acquired during 27.5-h $< t <$ 31-h and 43-h $< t <$ 48-h.
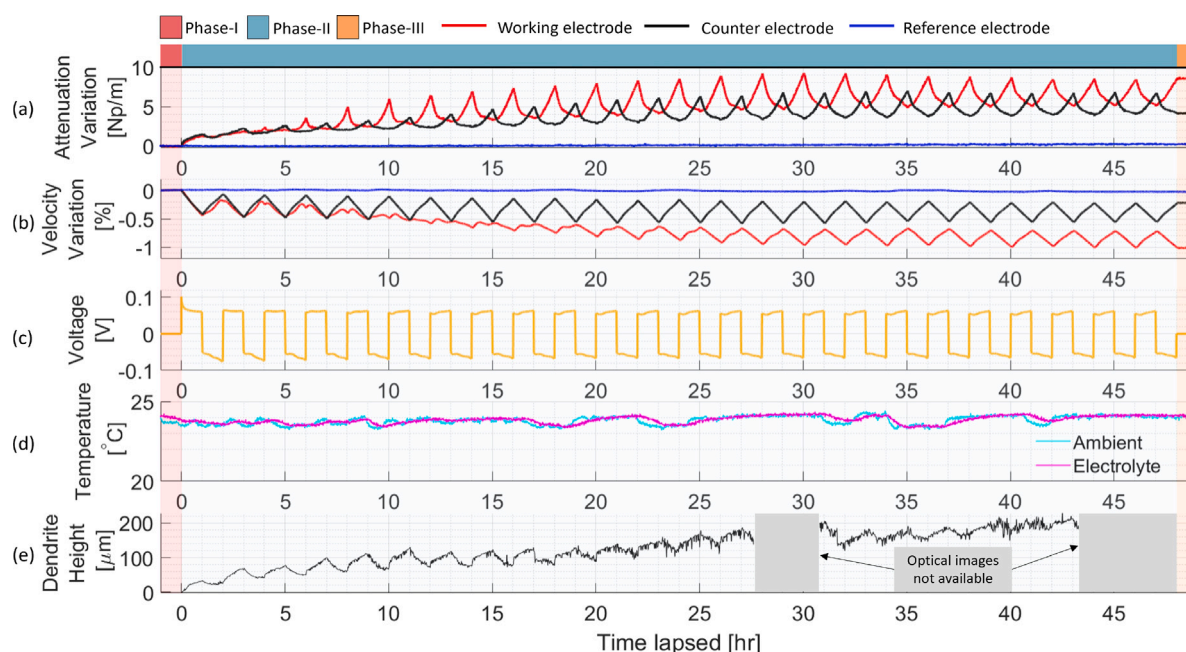
Fig. 4. (a) Temporal evolution of the wave attenuation on the three electrodes throughout the experiment. Time lapsed is synchronised with respect to the start of the cycling experiment. Periods correspond to Phase-I, -II, and -III of the experiment are shaded in light red, blue and yellow, respectively. (b) Evolution of wave velocity on the three electrode. (c) Variations of voltage difference across the working and counter electrode. (d) Measurements of ambient and electrolyte temperature. (e) Dendrite height evolution on the counter electrode. Estimates for dendrite height were not available because the image acquisition routine was disrupted in the two periods. The ultrasonic and electrochemical data was acquired using different hardware and therefore were not disrupted during the period. (For interpretation of the references to colour in this figure legend, the reader is referred to the web version of this article.)
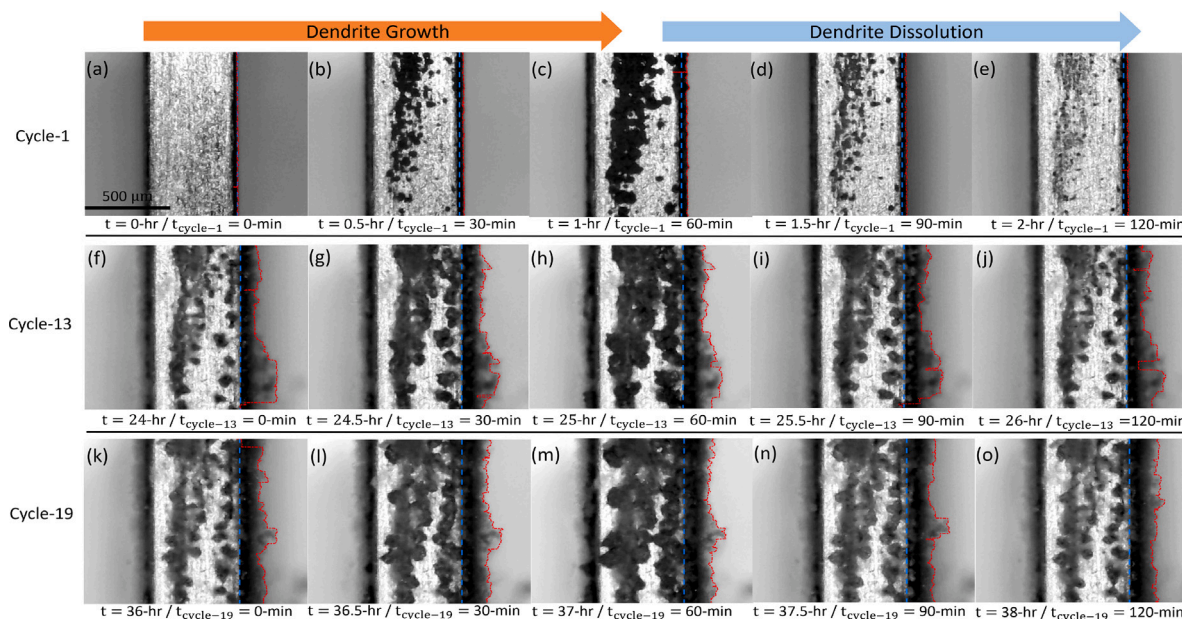

Fig. 5. Optical microscope images showing dendrite growth and dissolution on the cross section of counter electrode. Top row: cycle-1, middle row: cycle-13, bottom row: cycle-19. The red dash–dot lines mark the boundary between the electrode–dendrite complex and the background. The blue dashed lines mark the initial position of the electrode edge at the start of cycling at t=0-h. (For interpretation of the references to colour in this figure legend, the reader is referred to the web version of this article.)

Supplementary videos S1, S2 and S3 (Appendix A: Supplementary Information) were generated from the microscope images and ultrasonic measurement acquired between 0-h < t < 10-h, 10-h < t < 20-h and 31-h < t < 41-h. The video shows the zinc plating/stripping progress and was synchronised with the temporal evolution of ultrasonic and voltage measurements on the counter electrode to demonstrate the correlations between dendrite growth and changes in ultrasonic wave properties.

The electrodes were removed from the electrolyte at the end of Phase III for analysis. The cycled electrodes were washed gently with de-ionised water and dried in the air. Fig. 6(a) – 6(f) compare the states of three electrodes before and after the experiment. The reference electrode which did not take part in the electro-chemical reactions remained largely unchanged after the experiment; dark grey/black zinc dendrites can be observed on the working and counter electrode. There are more Zn dendrites on the working electrode than on the counter electrode. This is consistent with the inference based on the ultrasonic
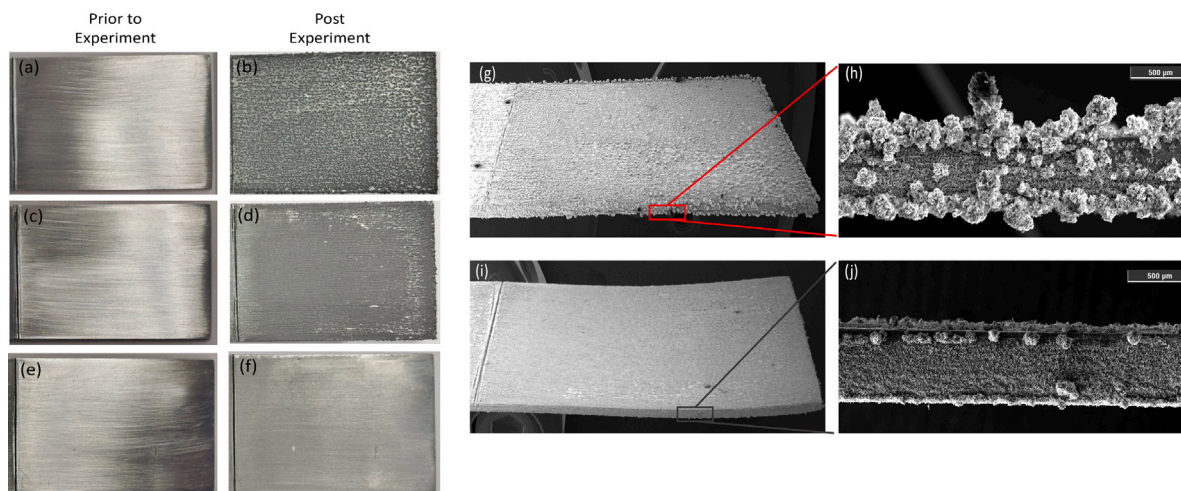
Fig. 6. Conditions of the working section of the electrodes before and after the cycling experiment: working electrode (a)–(b), counter electrode (c)–(d), and reference electrode (e)–(f). SEM images of zinc dendrites on the working electrode (g)–(h) and on the counter electrode (i)–(j).

measurements. Fig. 6(g) – 6(j) show some SEM images which provide further information on the scale of Zn dendrites on the working and counter electrode.

The phenomenon of asymmetric degradation of metal electrodes in symmetric cells has been reported by several researchers recently [19–21]. For instance, Koo et al. [19] observed that the reversibility of Li plating/stripping was higher on the initially-plated Li metal electrode (counter electrode) than on the initially-stripped Li metal electrode (working electrode). Longer Li dendrites were observed on the initially-stripped Li electrode, which also showed worse electrochemical performance. Koo et al. attributed the asymmetric behaviour to the different surface morphologies after the first half-cycle: the initially-stripped electrode has sharp and porous structures on the surface which are prone to dendrite growth. We believe the observed asymmetric behaviour of the ultrasonic measurements in this study were caused by similar morphology difference on the zinc electrode surface.

3.3. Intuitive interpretation of the results

Fig. 7 presents a graphical illustration of the mechanisms behind the evolution of ultrasonic wave attenuation and velocity. On a smooth waveguide (Fig. 7(a)), the shear waves will only couple very weakly with the surrounding electrolyte and additional wave attenuation and velocity due to shear leakage are minimal.

The electrode–electrolyte coupling increases once the cycling starts (Fig. 7(b) and 7(c)). Although different electro-chemical reactions happened on the surface of the working and counter electrodes, both reactions increased the 'surface roughness' of the electrodes relative to their initial pristine state. On the counter electrode, zinc plating lead to the porous and spongy dendrite complex. On the working electrode, zinc stripping acts like 'corrosion' and also left a sharp and porous structures on the electrode surface. Both morphological changes will increase the surface area and lead to the keying effect that converts shear wave motions into shear and pressure waves in the electrolyte. These translate into additional energy radiation into the electrolyte and thus increased attenuation [22]. On the other hand, both surface morphologies also impede the wave propagation by introducing additional mass/inertia adhered to the electrode surface. The added mass include not only the mass of zinc dendrites but also the electrolyte that is trapped in the porous structures on the waveguide surface. There are several literature sources that report and quantify the guide-wave slow-down due to liquid loading [18,23]. Together these explain why ultrasonic measurements on the two electrodes are observed to vary 'in phase' at the beginning of cycling despite opposite electrochemical reactions.

As the cycling continued (Fig. 7(d) and 7(e)), zinc dendrite growth/dissolution caused by the plating/stripping processes gradually dominated the change in surface morphology. As a result, we observed clear mirroring variations in attenuations and velocity between the two electrodes in the later stage of the cycling. Lastly, the asymmetric accumulated attenuation and velocity variations between the two electrode can be explained by the asymmetric dendrite growth as per the observation of Koo et al. [19] and the post-mortem microscopy.

3.4. Further experimental verification by removal of dendrites

To further verify that the observed attenuation and velocity variations are indeed caused by zinc dendrites grown on the electrode surface, the three electrodes were 'cleaned' by surface grinding with P2500 silicon carbide abrasive papers. The electrodes were reassembled with the test vessel and ultrasonic measurements were taken on the 'cleaned' electrodes. As shown in Fig. 8, most of the electrode surfaces have been restored to a state similar to that prior to the cycling experiment, some residuals which cannot be removed by surface grinding are believed to be 'corrosion pits'. Post cleaning (49-h < *t* < 50-h), dendrite-induced wave attenuation on the working and counter electrode reduced by approximately 70% and 55%, respectively; meanwhile, wave velocity variations on both electrodes are also observed to recover from that at the end of Phase-III, velocity reduction on the working electrode recovered by approximately 65% while the wave velocity on the counter electrode returned to its state prior to the cycling experiment. This directly proves that the observed increase in attenuation and reduction in velocity were the results of the presence of zinc dendrites on the electrode surfaces.

3.5. Discussion

It should be noted that the value of estimated dendrite height presented in Fig. 4(e) is only qualitative, and we do not seek to build quantitative correlations between dendrite height and ultrasonic wave properties here. This is because insufficient information about Zn dendrite distribution and morphology can be obtained from the optical microscope as it focused on a very small area (1 mm×0.5 mm) of the electrode whereas ultrasonic waves interrogated a much larger 3D volume (20 mm × 15 mm × 0.5 mm). The correlation between ultrasonic wave properties, especially the accumulated monotonic drift, and dendrite height estimates seems stronger in the initial charge/discharge cycles because zinc plating (dendrite growth) was relatively uniform in the early phase of the cycling. Hence, the optical image is more
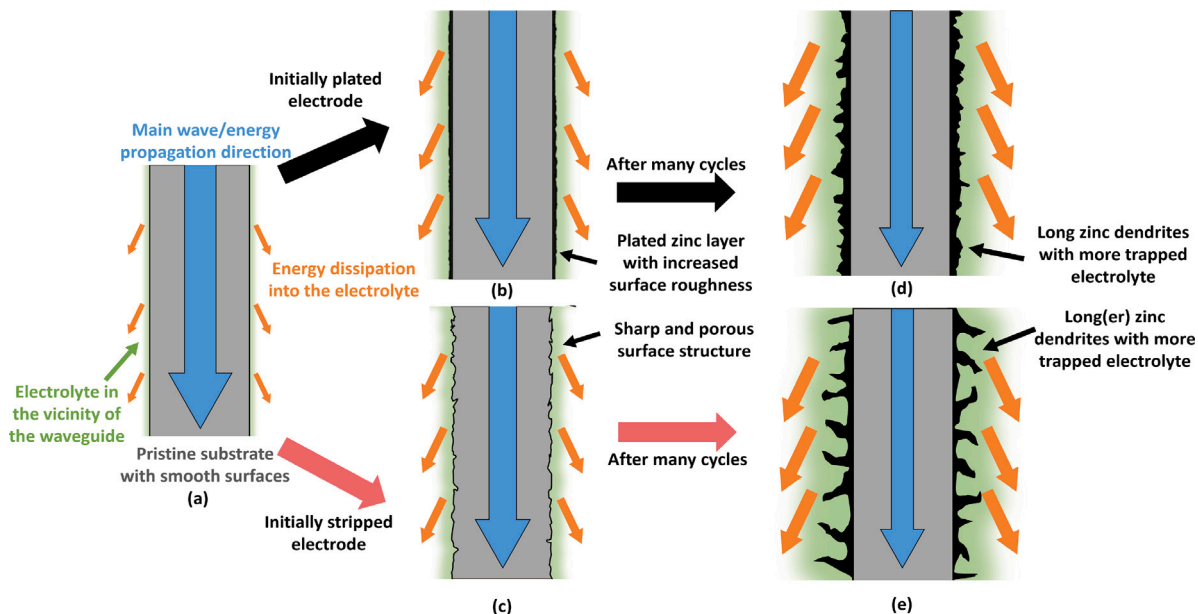
Fig. 7. Schematics of the dendrite growing process and ultrasonic sensing mechanisms. (a) The smooth, pristine electrode showing very weak coupling with the surrounding electrolyte and little energy dissipation. (b) The initially-plated electrode showing increased solid–liquid coupling and energy dissipation due to the plated rough zinc layer. (c) The initially-stripped electrode showing increasing solid–liquid coupling and energy dissipation due to its rough, porous surface morphology. (d) The initially-plated electrode after many cycles - zinc dendrites grown on the electrode surface causes considerable shear leakage and energy dissipation into the electrolyte. (e) The initially-stripped electrode after many cycles - (longer) zinc dendrites grown on the electrode surface causes even more shear leakage and energy dissipation into the electrolyte.
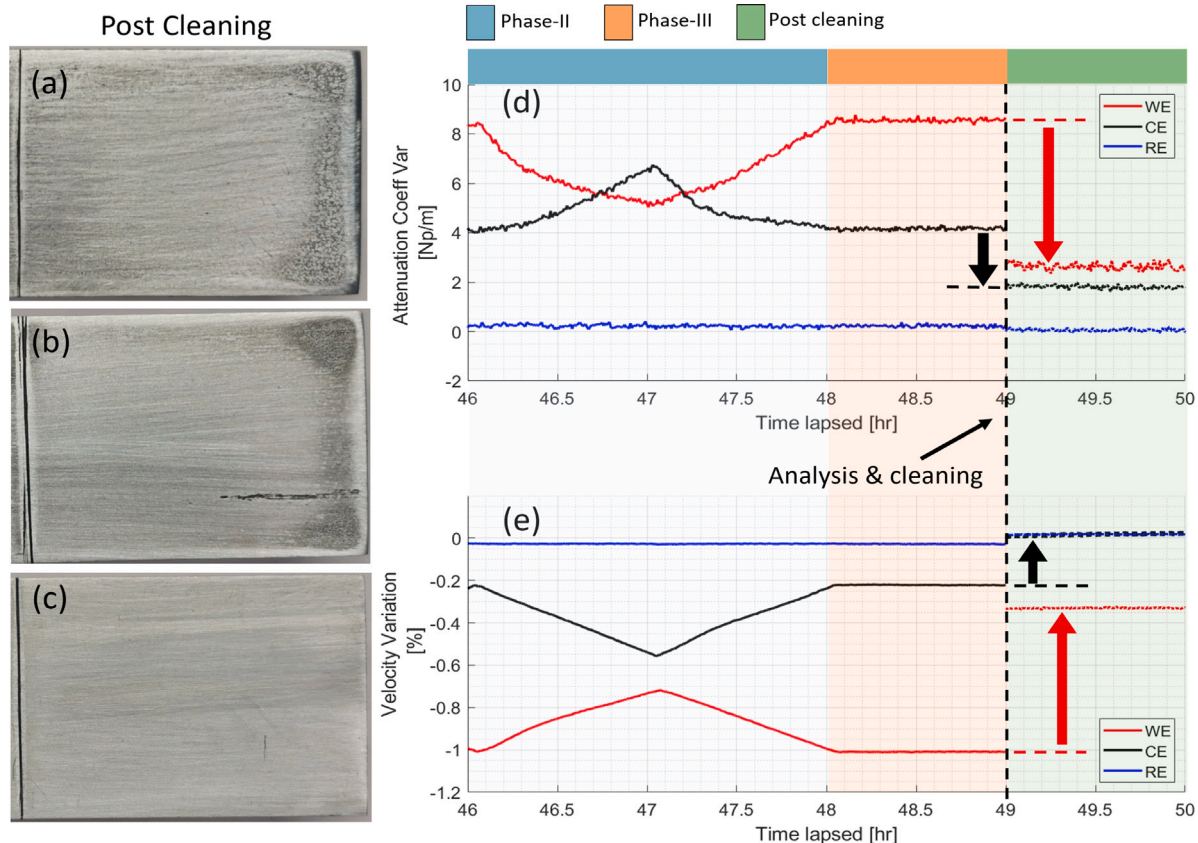

Fig. 8. Conditions of the (a) working electrode, (b) counter electrode, and (c) reference electrodes after the post-experiment cleaning. (d) Ultrasonic wave attenuation on the working and counter electrode showing a significant reduction after the cleaning (surface grinding). Cleaning was performed at the end of Phase-III at t = 49 h. The time lapsed during analysis and cleaning is omitted. (e) Ultrasonic wave velocity on the working and counter electrode showing a significant increase (recovery) after the cleaning. Because the CE and RE lines in Fig. 8e overlap, for these curves the data traces prior to cleaning are displayed using solid lines while the post-cleaning data traces are displayed using dotted lines.

representative of the average conditions of the electrode. However, as the cycling continued dendrite growth and distribution became increasingly inhomogeneous and hence the optical images were less representative of the average conditions of the electrode, and the correlation between ultrasonic wave properties and observed dendrite height appears to be less strongly related (i.e. reduced apparent sensitivity of the ultrasonic technique at the later phase of the experiment).

In addition, the estimates of dendrite height are inferred from the images acquired from the optical microscope, which are essentially the projections of Zn dendrite over the depth of view of the microscope on a 2-D plane. If the Zn dendrite distribution across the depth of view is inhomogeneous, as in the case at the later phase of the cycling, the variations of dendrite height on the 2-D image will be larger than the true average value in the 3-D space (i.e. over the electrode surface) and also larger than the variations of ultrasonic wave properties. This effect also leads to the reduced apparent correlation between the ultrasonic wave properties and the estimated dendrite height at the later phase of the experiment.

The sensitivity and resolution of the presented ultrasonic technique will be a key factor determining its usefulness for battery/electrode health monitoring. Since the optical microscopy currently being employed was unable to provide volumetric information on dendrite distribution and tomography, X-ray CT will be employed in the subsequent investigations to gather information on dendrite distribution. In addition, since dendrite distribution is closely related to the initial surface roughness of the electrode [24], numerical models [25,26] that simulate ultrasound–dendrite–electrolyte interactions can be built to provide more physical intuition and quantitative correlations between ultrasonic wave properties and dendrite formation. With that it is also possible to formulate inverse relationships between ultrasonic wave signals and dendrite tomography. Further studies will also be carried out with full cell systems and under different conditions.

4. Conclusions

In this study we present a novel ultrasound-based method for in-situ monitoring of dendrite formation (electrode degradation) in a symmetric aqueous zinc cell system. We demonstrated that zinc plating/stripping that was cyclically imposed on the working and counter electrode can be clearly observed from the attenuation and velocity variations of the SH0* mode ultrasonic waves. This confirmed our hypothesis that this guided wave shows good sensitivity to dendrite formation at the electrode interface. The formation of zinc dendrite (dead zinc) can be associated with a monotonic increase in wave attenuation and an accompanying reduction in wave velocity.

While the technique showed clear correlations between guided ultrasonic wave properties and zinc dendrites in the initial plating/stripping cycles, the apparent correlations were observed to subdue in the later stage of the cycling experiment. Quantitative assessments of its sensitivity and improvement of its resolution will be a key focus of future investigations. A hybrid approach of experimental modification, verification and numerical simulation is suggested.

Compared with conventional ultrasonic techniques, the presented method is capable of interrogating individual electrodes separately. Thus, it offers valuable insights into the physical changes that take place on the electrode surface, allowing researchers to investigate the underlying mechanisms of electrode degradation. The method can be applied to other metal-electrode batteries (e.g. lithium-metal batteries and zinc-air batteries) which are also subjected to the risk of dendrite induced failures.

The presented method is very versatile such that it can be used at the electrode level in a laboratory, as demonstrated in this study. Furthermore, it can also be integrated into commercial batteries for long-term, *in-situ*, and real-time monitoring. More importantly, this method provides quantitative monitoring data that can be associated with physical changes on the electrodes. In summary, we believe the presented principle can inspire more quantitative research into *in-situ-/operando* monitoring of dendrite formation and electrode health in batteries.

CRediT authorship contribution statement

Yifeng Zhang: Conceptualization, Methodology, Investigation, Formal analysis, Data curation, Writing – original draft. **Haobo Dong:** Conceptualization, Methodology, Investigation, Writing – original draft. **Tianlei Wang:** Investigation. **Guanjie He:** Supervision, Writing – review & editing. **Ivan P. Parkin:** Supervision, Writing – review & editing. **Frederic Cegla:** Supervision, Methodology, Writing – review & editing.

Declaration of competing interest

The authors declare that they have no known competing financial interests or personal relationships that could have appeared to influence the work reported in this paper.

Appendix A. Supplementary information

Supplementary material related to this article can be found online at https://doi.org/10.1016/j.jpowsour.2022.231730.

References

[1] H. Dong, J. Li, J. Guo, F. Lai, F. Zhao, Y. Jiao, D.J. Brett, T. Liu, G. He, I.P. Parkin, Insights on flexible zinc-ion batteries from lab research to commercialization, Adv. Mater. 33 (20) (2021) http://dx.doi.org/10.1002/adma.202007548.

[2] D. Kundu, B.D. Adams, V. Duffort, S.H. Vajargah, L.F. Nazar, A high-capacity and long-life aqueous rechargeable zinc battery using a metal oxide intercalation cathode, Nat. Energy 1 (10) (2016) 1–8, http://dx.doi.org/10.1038/nenergy.2016.119.

[3] J. Shin, J. Lee, Y. Park, J.W. Choi, Aqueous zinc ion batteries: Focus on zinc metal anodes, Chem. Sci. 11 (8) (2020) 2028–2044, http://dx.doi.org/10.1039/d0sc00022a.

[4] J. Hao, X. Li, X. Zeng, D. Li, J. Mao, Z. Guo, Deeply understanding the Zn anode behaviour and corresponding improvement strategies in different aqueous Zn-based batteries, Energy Environ. Sci. 13 (11) (2020) 3917–3949, http://dx.doi.org/10.1039/d0ee02162h.

[5] C.J. Huang, B. Thirumalraj, H.C. Tao, K.N. Shitaw, H. Sutiono, T.T. Hagos, T.T. Beyene, L.M. Kuo, C.C. Wang, S.H. Wu, W.N. Su, B.J. Hwang, Decoupling the origins of irreversible coulombic efficiency in anode-free lithium metal batteries, Nature Commun. 12 (1) (2021) 1–10, http://dx.doi.org/10.1038/s41467-021-21683-6.

[6] S. Higashi, S.W. Lee, J.S. Lee, K. Takechi, Y. Cui, Avoiding short circuits from zinc metal dendrites in anode by backside-plating configuration, Nature Commun. 7 (2016) 1–6, http://dx.doi.org/10.1038/ncomms11801.

[7] V. Yufit, F. Tariq, D.S. Eastwood, M. Biton, B. Wu, P.D. Lee, N.P. Brandon, Operando visualization and multi-scale tomography studies of dendrite formation and dissolution in zinc batteries, Joule 3 (2) (2019) 485–502, http://dx.doi.org/10.1016/j.joule.2018.11.002.

[8] Z. Guo, J. Zhu, J. Feng, S. Du, Direct in situ observation and explanation of lithium dendrite of commercial graphite electrodes, RSC Adv. 5 (85) (2015) 69514–69521, http://dx.doi.org/10.1039/c5ra13289d.

[9] C. Shen, G. Hu, L.Z. Cheong, S. Huang, J.G. Zhang, D. Wang, Direct observation of the growth of lithium dendrites on graphite anodes by operando EC-AFM, Small Methods 2 (2) (2018) 1–7, http://dx.doi.org/10.1002/smtd.201700298.

[10] J.B. Robinson, M. Maier, G. Alster, T. Compton, D.J.L. Brett, P.R. Shearing, Spatially resolved ultrasound diagnostics of li-ion battery electrodes, Phys. Chem. Chem. Phys. 21 (2019) 6354–6361, http://dx.doi.org/10.1039/C8CP07098A.

[11] J.B. Robinson, M. Pham, M.D. Kok, T.M. Heenan, D.J. Brett, P.R. Shearing, Examining the cycling behaviour of li-ion batteries using ultrasonic time-of-flight measurements, J. Power Sources 444 (October) (2019) 227318, http://dx.doi.org/10.1016/j.jpowsour.2019.227318.

[12] M.T. Pham, J.J. Darst, D.P. Finegan, J.B. Robinson, T.M. Heenan, M.D. Kok, F. Iacoviello, R. Owen, W.Q. Walker, O.V. Magdysyuk, T. Connolley, E. Darcy, G. Hinds, D.J. Brett, P.R. Shearing, Correlative acoustic time-of-flight spectroscopy and X-ray imaging to investigate gas-induced delamination in lithium-ion pouch cells during thermal runaway, J. Power Sources 470 (June) (2020) 228039, http://dx.doi.org/10.1016/j.jpowsour.2020.228039.

[13] W. Chang, R. Mohr, A. Kim, A. Raj, G. Davies, K. Denner, J.H. Park, D. Steingart, Measuring effective stiffness of Li-ion batteries: Via acoustic signal processing, J. Mater. Chem. A 8 (32) (2020) 16624–16635, http://dx.doi.org/10.1039/d0ta05552b.

[14] C. Bommier, W. Chang, Y. Lu, J. Yeung, G. Davies, R. Mohr, M. Williams, D. Steingart, In operando acoustic detection of lithium metal plating in commercial LiCoO2/Graphite pouch cells, Cell Rep. Phys. Sci. 1 (4) (2020) 100035, http://dx.doi.org/10.1016/j.xcrp.2020.100035.

[15] G. Bucci, T. Swamy, S. Bishop, B.W. Sheldon, Y.-M. Chiang, W.C. Carter, The effect of stress on battery-electrode capacity, J. Electrochem. Soc. 164 (4) (2017) A645–A654, http://dx.doi.org/10.1149/2.0371704jes.

[16] F.B. Cegla, Energy concentration at the center of large aspect ratio rectangular waveguides at high frequencies, J. Acoust. Soc. Am. 123 (6) (2008) 4218–4226, http://dx.doi.org/10.1121/1.2908273.

[17] B. Herdovics, F. Cegla, Compensation of phase response changes in ultrasonic transducers caused by temperature variations, Struct. Health Monit. 18 (2) (2019) 508–523, http://dx.doi.org/10.1177/1475921718759272.

[18] J. Huang, F. Cegla, A. Wickenden, M. Coomber, Simultaneous measurements of temperature and viscosity for viscous fluids using an ultrasonic waveguide, Sensors 21 (16) (2021) http://dx.doi.org/10.3390/s21165543.

[19] D. Koo, B. Kwon, J. Lee, K.T. Lee, Asymmetric behaviour of Li/Li symmetric cells for Li metal batteries, Chem. Commun. 55 (65) (2019) 9637–9640, http://dx.doi.org/10.1039/c9cc04082j.

[20] H. Liu, X.B. Cheng, R. Xu, X.Q. Zhang, C. Yan, J.Q. Huang, Q. Zhang, Plating/stripping behavior of actual lithium metal anode, Adv. Energy Mater. 9 (44) (2019) 1–7, http://dx.doi.org/10.1002/aenm.201902254.

[21] Y.K. Huang, R. Pan, D. Rehnlund, Z. Wang, L. Nyholm, First-cycle oxidative generation of lithium nucleation sites stabilizes lithium-metal electrodes, Adv. Energy Mater. 11 (9) (2021) 1–13, http://dx.doi.org/10.1002/aenm.202003674.

[22] F.B. Cegla, P. Cawley, M.J.S. Lowe, Material property measurement using the quasi-scholte mode—A waveguide sensor, J. Acoust. Soc. Am. 117 (3) (2005) 1098–1107, http://dx.doi.org/10.1121/1.1841631.

[23] J.O. Kim, H.H. Bau, Instrument for simultaneous measurement of density and viscosity, Rev. Sci. Instrum. 60 (6) (1989) 1111–1115, http://dx.doi.org/10.1063/1.1140325.

[24] Z. Zhang, S. Said, K. Smith, Y.S. Zhang, G. He, R. Jervis, P.R. Shearing, T.S. Miller, D.J. Brett, Dendrite suppression by anode polishing in zinc-ion batteries, J. Mater. Chem. A 9 (27) (2021) 15355–15362, http://dx.doi.org/10.1039/d1ta02682h.

[25] G. Sarris, S.G. Haslinger, P. Huthwaite, P.B. Nagy, M.J.S. Lowe, Attenuation of Rayleigh waves due to surface roughness, J. Acoust. Soc. Am. 149 (6) (2021) 4298–4308, http://dx.doi.org/10.1121/10.0005271.

[26] T. Grabec, I.A. Veres, M. Ryzy, Surface acoustic wave attenuation in polycrystals: Numerical modeling using a statistical digital twin of an actual sample, Ultrasonics 119 (September 2021) (2022) 106585, http://dx.doi.org/10.1016/j.ultras.2021.106585.